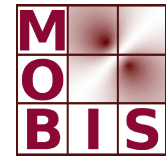
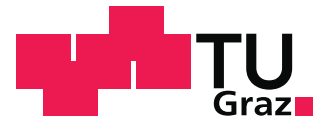




SpezialForschungsBereich F 32



Karl-Franzens Universität Graz
Technische Universität Graz
Medizinische Universität Graz



Efficient computation of electrograms and ECGs in human whole heart simulations using a reaction-eikonal model

A. Neic F. O. Campos A. J. Prassl
S. A. Niederer M. J. Bishop E. J. Vigmond
 G. Plank

SFB-Report No. 2017-002

February 2017

A-8010 GRAZ, HEINRICHSTRASSE 36, AUSTRIA

Supported by the
Austrian Science Fund (FWF)



SFB sponsors:

- **Austrian Science Fund (FWF)**
- **University of Graz**
- **Graz University of Technology**
- **Medical University of Graz**
- **Government of Styria**
- **City of Graz**



Efficient computation of electrograms and ECGs in human whole heart simulations using a reaction-eikonal model

Aurel Neic Fernando O. Campos Anton J. Prassl Steven A. Niederer
Martin J. Bishop Edward J. Vigmond Gernot Plank

February 10, 2017

Abstract

Anatomically accurate and biophysically detailed bidomain models of the human heart have proven a powerful tool for gaining quantitative insight into the links between electrical sources in the myocardium and the concomitant current flow in the surrounding medium as they represent their relationship mechanistically based on first principles. Such models are increasingly considered as a clinical research tool with the perspective of being used, ultimately, as a complementary diagnostic modality. An important prerequisite in many clinical modeling applications is the ability of models to faithfully replicate potential maps and electrograms recorded from a given patient. However, while the personalization of electrophysiology models based on the gold standard bidomain formulation is in principle feasible, the associated computational expenses are significant, rendering their use incompatible with clinical time frames.

In this study we report on the development of a novel computationally efficient reaction-eikonal (R-E) model for modeling extracellular potential maps and electrograms. Using a biventricular human electrophysiology model, which incorporates a topologically realistic His-Purkinje system (HPS), we demonstrate by comparing against a high-resolution reaction-diffusion (R-D) bidomain model that the R-E model predicts extracellular potential fields, electrograms as well as ECGs at the body surface with high fidelity and offers vast computational savings greater than three orders of magnitude. Due to their efficiency R-E models are ideally suitable for forward simulations in clinical modeling studies which attempt to personalize electrophysiological model features.

Keywords: Cardiac Electrophysiology, Bidomain Model, Eikonal Model, Electrical Activation and Repolarization.

1 Introduction

The ability to monitor electrical activation and repolarization sequences in the human heart is of fundamental importance for understanding cardiac function under healthy conditions, and plays a pivotal role in the clinical diagnosis and treatment of cardiac diseases. These sequences – often visualized as isochronal maps on the heart or body surface built from recorded instants in time which indicate specific local events representative of depolarization or repolarization – are determined by the spatio-temporal distribution of the intrinsic bioelectric sources throughout the myocardium.

These sources are the transmembrane currents which enter or leave a cell and thus alter the transmembrane voltages governing the dynamics of myocytes and also set up potential fields in the intra- and extracellular spaces.

A direct observation of bioelectric sources *in vivo* is currently not feasible. The clinical assessment of electrophysiological aspects of cardiac diseases relies almost exclusively upon the indirect observation of extracellular potentials. The time course of these potentials – referred to as electrograms – are recorded within the body, which acts as an extensive volume conductor. Thus they provide only a filtered non-unique view on the intrinsic sources, which can render their interpretation a challenging task. The degree of filtering depends largely on the distance of a recording electrode to the sources within the myocardial walls as well as conductivity and heterogeneities within the surrounding medium. Such electrogram recordings are ubiquitous in clinical electrophysiological examinations, be it by means of electrodes in implantable devices, with catheters during interventions or with electrical mapping systems which record electrograms synchronously at multiple sites to reconstruct spatio-temporal maps of the extracellular potential field.

A thorough understanding of the mechanisms underlying the genesis of extracellular potential fields within the human body and their relation to the electrical sources within the myocardium is therefore key for the sound construction of activation and repolarization maps, their interpretation and the therapeutic decisions based on it. *In-silico* computer models show high promise as a tool for gaining a better quantitative insight into the mechanisms which link cardiac sources to their signature in extracellular potential fields. Anatomically accurate and biophysically detailed bidomain models of the human heart and a surrounding torso are considered the gold standard for such *forward* electrophysiological modeling studies due to their ability to faithfully replicate organ-scale electrophysiology by representing both electrical sources and the concomitant current flow they induce in the interstitial and extracellular spaces. While such simulations have become feasible [42], the associated computational costs are significant due to the reaction-diffusion (R-D) nature of the bidomain model which imposes stability and accuracy constraints on spatio-temporal discretization schemes. These costs are considered a limiting factor, effectively restricting the use of such models to highly specialized research software which is able to efficiently exploit current high performance computing (HPC) infrastructure to keep simulations tractable [34, 31, 45].

Virtually all scenarios considering the clinical application of *in-silico* models critically depend on the ability of personalizing models to provide complementary input for diagnosis [33], disease stratification [2], therapy optimization, planning and outcome prediction in a patient-specific manner. Such applications require a substantial number of forward simulations as these are integrated in an optimization loop where often sizable parameters spaces must be explored to iteratively reparameterize models until a sufficiently close match with clinical data is achieved. Typically, in such scenarios the use of R-D models is punitively expensive and thus not easily reconcilable with the constraints imposed by clinical workflows. Computationally cheaper models which yield electrograms of the same or at least of comparable electrophysiological fidelity are therefore sought after as a fundamental key technology for leveraging *in-silico* modeling in the clinic.

Significant computational savings can be achieved if the spatio-temporal evolution of cardiac sources within the myocardium can be represented accurately using coarser mesh resolutions. The eikonal model [14, 27] has become a popular choice in applications where maps of cardiac activation and repolarization are to be modeled [38, 24, 12]. In this study we further advance this idea by investigating the appropriateness of a reaction-eikonal (R-E) source model for computing electrograms and ECGs which offers the computational advantages of the eikonal model while preserving the full biophysical details of a computationally costly reaction-diffusion (R-D) model. Coupling is

achieved by triggering the reaction model through the injection of physiologically motivated stimulus currents in a modified monodomain or pseudo-bidomain model at the instants of depolarization wavefront arrival times as provided by the eikonal model [14, 27]. These trigger currents raise the transmembrane voltage following the foot of a propagated action potential in the same way as in a full-blown bidomain R-D model. Particular emphasis was put on the coupling of biophysically detailed reaction terms to eikonal-based activation as to ascertain that upstroke and early repolarization phase of the action potential remained unaffected and that repolarization gradients were adequately preserved.

Using a biventricular human electrophysiology model, which also incorporates a topologically realistic His-Purkinje system (HPS), we demonstrate by comparing against a high-resolution R-D bidomain model that the R-E model predicts extracellular potential maps and electrograms in the vicinity of myocardial surfaces as well as ECGs at the body surface with high fidelity at a vastly reduced computational expense. Computational savings greater than three orders of magnitude could be achieved without any appreciable deviations or any reduction in biophysical detail as compared to a full-blown R-D bidomain model. The achieved computational savings stem mainly from relaxed spatial resolution constraints as the R-E models yield converged activation patterns at coarser spatial resolutions. Due to their efficiency, R-E models are ideally suitable for forward simulations in clinical modeling studies which attempt to replicate electrophysiological recordings in the clinic or to efficiently personalize electrophysiological model features.

2 Methods

2.1 Bidomain Model

The bidomain equations state that transmembrane currents, I_m , that enter intracellular and extracellular spaces by crossing the cell membrane, represent sources for intracellular, Φ_i , and extracellular, Φ_e , potentials and are given by

$$\nabla \cdot \boldsymbol{\sigma}_i \nabla \Phi_i = \beta I_m \quad (1)$$

$$\nabla \cdot \boldsymbol{\sigma}_e \nabla \Phi_e = -\beta I_m - I_{ei} \quad (2)$$

$$I_m = C_m \frac{\partial V_m}{\partial t} + I_{ion}(V_m, \boldsymbol{\eta}) - I_s \quad (3)$$

$$\frac{\partial \boldsymbol{\eta}}{\partial t} = f(\boldsymbol{\eta}, t) \quad (4)$$

$$\nabla \cdot \boldsymbol{\sigma}_b \nabla \Phi_e = -I_{eb} \quad (5)$$

where $V_m = \Phi_i - \Phi_e$ is the transmembrane voltage, $\boldsymbol{\sigma}_i$ and $\boldsymbol{\sigma}_e$ are the intracellular and extracellular conductivity tensors, respectively, β is the bidomain membrane surface-to-volume ratio, I_{ei} and I_{eb} are extracellular stimuli applied in the interstitial space or the bath, respectively, I_s is a transmembrane stimulus current, C_m is the membrane capacitance per unit area, and I_{ion} is the membrane ionic current density which depends on V_m and a set of state variables, $\boldsymbol{\eta}$.

Equations (1)–(5) can be recast and solved in the elliptic-parabolic form given by

$$\begin{bmatrix} -\nabla \cdot (\boldsymbol{\sigma}_i + \boldsymbol{\sigma}_e) \nabla \Phi_e \\ -\nabla \cdot \boldsymbol{\sigma}_b \nabla \Phi_e \end{bmatrix} = \begin{bmatrix} \nabla \cdot \boldsymbol{\sigma}_i \nabla V_m + I_{ei} \\ I_{eb} \end{bmatrix} \quad (6)$$

$$\beta C_m \frac{\partial V_m}{\partial t} = \nabla \cdot \boldsymbol{\sigma}_i \nabla \Phi_i - \beta (I_{ion}(V_m, \boldsymbol{\eta}) - I_s). \quad (7)$$

At the tissue-bath interface, that is the interface between interstitial space of the myocardium and blood pool or the surrounding torso, no flux boundary conditions are approximated for Φ_i , as well as continuity of Φ_e and the normal component of the extracellular current. At the boundaries formed by the surrounding medium, i.e. either the body surface or the boundary of a bath, no flux boundary conditions for Φ_e are imposed. The full bidomain model thus provides the most physiologically-realistic representation of cardiac bioelectric activity at the organ scale, yielding V_m and Φ_e at every point in space and time, as well as implicitly accounting for the effects of bath-loading upon wavefront dynamics through representation of a surrounding conductive media such as blood pool or torso.

2.2 Pseudo-bidomain Model

A pseudo-bidomain model approximates a full-blown bidomain model with high accuracy, but at a fraction of the computational costs. The derivation of the pseudo-bidomain model was reported in detail elsewhere [6, 7]. Briefly, assuming that the intra- and extracellular domains are both anisotropic, but to the same degree, that is, $\sigma_e = \lambda \sigma_i$ holds with λ being a scalar, the bidomain equations can be reduced to the monodomain equation [36] by inserting this relation into Eqs. (1) & (2). This yields

$$C_m \frac{\partial V_m}{\partial t} + I_{\text{ion}} = \nabla \cdot (\sigma_m \nabla V_m), \quad (8)$$

where σ_m is the harmonic mean conductivity tensor or the effective *bulk conductivity*, which leads to an accurate match in conduction velocities between bidomain and monodomain model along the tissue's principal eigenaxes [15].

As shown previously [6], bath-loading effects as observed in bidomain models are closely reproduced with monodomain models if the conductivity tensor σ_m in Eq. (8) is represented by σ_m^* , where the * signifies either *b* in the tissue bulk or *s* along the surfaces. In the tissue bulk the eigenvalues of σ_m^* are given as

$$\sigma_m^{b\zeta} = \frac{\sigma_i^\zeta \sigma_e^\zeta}{\sigma_i^\zeta + \sigma_e^\zeta}, \quad (9)$$

where $\zeta = l|t|n$ are the eigendirections of the tissue along the cardiac fiber direction ($\zeta = l$), transverse ($\zeta = t$) to the fibers within a sheet, and along a sheet normal direction ($\zeta = n$). In the myocardial tissue close to the tissue-bath interface a thin augmentation layer is defined within which it is assumed that extracellular conductivity is rather governed by the bath conductivity σ_b than the interstitial conductivity σ_e thus the conductivity tensor in the augmentation layer is given by

$$\sigma_m^{s\zeta} = \frac{\sigma_i^\zeta \sigma_b}{\sigma_i^\zeta + \sigma_b}. \quad (10)$$

As shown previously [6], this *augmented monodomain* approach faithfully accounts for bath-loading whilst, as it is computationally just a monodomain model, only representing $V_m(\mathbf{x}, t)$. Using $V_m(\mathbf{x}, t)$ as computed with an augmented monodomain as a right hand side of Eq.(6), allows the computation of extracellular potential fields $\Phi_e(\mathbf{x}, t)$ within both interstitial Ω_e as well as bath domain Ω_b , respectively. This coupling of an augmented monodomain model with the elliptic portion of the bidomain model in Eq. (6) is referred to as *pseudo-bidomain* model as it predicts the same activation sequence as a bidomain model, albeit at a much cheaper computational cost, and provides realistic

extracellular potential fields in a bounded medium surrounding the heart. The computational complexity of the pseudo-bidomain model is only marginally higher than a monodomain model as the elliptic equation (6) is solved infrequently at those instances which correspond to a specified temporal output granularity. A detailed account on the limitations of the pseudo-bidomain approach has been reported elsewhere [6, 7].

2.3 Spatio-temporal discretization

A Galerkin finite element approach using linear tetrahedral elements was used for spatial discretization of the domains Ω_i and Ω_e [47]. The HPS was discretized in space using cubic-hermite line elements [59]. Elliptic (6) and parabolic portions (7) of the bidomain equations are decoupled and solved sequentially [58]. Temporal discretization relied upon elliptic-parabolic decoupling and operator splitting of diffusion and reaction terms. That is, first the elliptic system (6) is solved, then an operator splitting approach is employed to subsequently solve the parabolic system [53, 44, 54]. This allows us to treat reaction and diffusion terms separately. The reaction term represented by the ODE system (4) is solved using an accelerated Rush–Larsen technique, see [40], and the diffusion problem is solved using a Crank–Nicolson scheme. Using $t^k = k\Delta t$ yields the following linear system of equations to obtain $(\underline{\phi}_e^{k+1}, \underline{V}_m^{k+1}, \underline{\eta}^{k+1}) \in \mathbb{R}^N \times \mathbb{R}^N \times \mathbb{R}^N$ such that

$$\mathbf{K}_{i+e} \underline{\phi}_e^{k+1} = -\mathbf{K}_i \underline{V}_m^k, \quad (11)$$

$$\underline{\eta}_f^{k+1} = \underline{\eta}_f^k e^{-\frac{\Delta t}{\tau}} + \underline{\eta}_{f\infty} \left(1 - e^{-\frac{\Delta t}{\tau}}\right) \quad (12)$$

$$\underline{\eta}_s^{k+1} = \underline{\eta}_s^k + \underline{g}(V_m^{k*}, \underline{\eta}_s^k) \Delta t \quad (13)$$

$$\underline{V}_m^{k+\frac{1}{2}} = \underline{V}_m^k - \frac{\Delta t}{C_m} I_{\text{ion}}(\underline{V}_m^k, \underline{\eta}^{k+1}), \quad (14)$$

$$(\widetilde{\mathbf{M}}_i + \frac{1}{2}\mathbf{K}_i)\underline{V}_m^{k+1} = -\mathbf{K}_i \left(\frac{1}{2}\underline{V}_m^{k+\frac{1}{2}} + \underline{\phi}_e^k\right) + \widetilde{\mathbf{M}}_i \underline{V}_m^{k+\frac{1}{2}}, \quad (15)$$

where

$$\mathbf{K}_{i+e}[j, i] := \int_{\Omega_0} (\sigma_i + \sigma_e) \nabla \varphi_i \nabla \varphi_j \, d\mathbf{X}, \quad (16)$$

$$\mathbf{K}_i[j, i] := \int_{\Omega_0} \sigma_i \nabla \varphi_i \nabla \varphi_j \, d\mathbf{X}, \quad (17)$$

$$\widetilde{\mathbf{M}}_i[j, i] := \frac{\beta C_m}{\Delta t} \int_{\Omega_0} \varphi_i \varphi_j \, d\mathbf{X}, \quad (18)$$

$\underline{\eta} = \{\underline{\eta}_f, \underline{\eta}_s\}$ with $\underline{\eta}_f$ being fast acting gating variables solved for by evaluating an analytical solution, τ and $\underline{\eta}_{f\infty}$ are functions of the rate coefficients which govern channel gating kinetics, and $\underline{\eta}_s$ are slower acting states, integrated with a forward Euler method [40]. From this construction and $\sigma_i = \sigma_i^\top$, $\sigma_e = \sigma_e^\top$ we conclude that the matrices (16–18) are symmetric and positive definite. The CG method is therefore applicable to solve the linear systems of equations (11) and (15).

2.4 Linear Solvers

All linear solvers used in this study were implemented in the publicly available numerical package Parallel Toolbox (pt) [29, 20]. The cardiac bidomain equations were solved in parallel using the

Cardiac Arrhythmia Research Package (CARP) [57] as an outer framework which was interfaced with the pt library. Technical aspects have been described elsewhere [32]. CARP makes use of the MPI based library PETSc [4] as the basic infrastructure for handling parallel matrices and vectors. Parallel partitioning of unstructured grids relies upon the graph based domain decomposition ParMetis [25, 26].

Details on the methods employed for solving the bidomain equations in parallel have been reported previously [39, 58, 32]. Briefly, the elliptic portion of the bidomain equations is solved using the algebraic multigrid preconditioner ptAMG [29] with an iterative CG solver method (ptAMG-PCG). The parabolic portion of the bidomain equation is solved using an ω -Jacobi preconditioner, also in combination with the iterative CG solver (ω J-PCG), using an ω of 2/3 and two iterations per CG iteration [32].

2.5 Eikonal Model

The eikonal model can be used to represent arrival times, t_a , of depolarization wavefronts in the myocardial domain Ω_i based on a spatially heterogeneous orthotropic velocity function encoded as $\mathbf{V}(\mathbf{x})$ and initial activations t_0 at locations Γ . The eikonal equation is of the form

$$\begin{cases} \sqrt{\nabla t_a^\top \mathbf{V} \nabla t_a} = 1 & \text{in } \Omega_i \\ t_a = t_0 & \text{in } \Gamma \end{cases} \quad (19)$$

where Ω_i is the myocardium, t_a is a positive function describing the wavefront arrival time at location \mathbf{x} and \mathbf{V} is a symmetric positive definite 3×3 tensor describing orthotropy of conduction velocity.

The eikonal equation is solved using a custom implementation of the Fast Iterative Algorithm [18] with further additions to facilitate the incorporation of a His-Purkinje System (HPS) and its coupling to the myocardium through Purkinje-ventricular junctions (PVJ), similar to an implementation reported in [38].

A finite-element-based tetrahedral tessellation was used to spatially discretize the domain Ω_i and line elements were used for discretizing the HPS. A PVJ is therefore represented as a vertex where a line element connects to a tetrahedron. Asymmetric delays in impulse transduction between PS and myocardium were taken into account with 10 *ms* and 3 *ms* in anterograde and retrograde direction, respectively [17, 10].

2.6 Reaction-Eikonal Model

Using an eikonal model $t_a(\mathbf{x})$ can be computed efficiently with sufficient accuracy at a lower spatial resolution and, thus, lower computational cost as compared to R-D models, which demand higher spatial resolutions due to numerical accuracy constraints [35]. This motivates a reaction-eikonal (R-E) model, where the propagation of depolarization wavefronts is mediated by eikonal-based activation maps and not by diffusion. Depolarization at site \mathbf{x} is initiated at time $t_a(\mathbf{x})$ by a prescribed stimulus current, I_{foot} , which is designed to depolarize the local membrane at \mathbf{x} above the activation threshold of the sodium current. The time course of $I_{\text{foot}}(t)$ is chosen to depolarize the membrane following the same foot of an action potential, $V_{\text{m,foot}}$, as otherwise mediated by diffusion in a R-D model. That is, the foot current in time is given by

$$I_{\text{foot}}(t) \approx -C_m \frac{\partial V_{\text{foot}}}{\partial t} \quad (20)$$

and in space by

$$I_{\text{foot}}(\mathbf{x}, t) := \begin{cases} I_{\text{foot}}(t) & \text{if } t \in [t_a(\mathbf{x}) - T_{\text{foot}}, t_a(\mathbf{x})] \\ 0 & \text{else} \end{cases} \quad (21)$$

A detailed rationale on the design of $I_{\text{foot}}(t)$ is given in the appendix. In the R-E model the current I_{foot} is either added as an additional stimulus current or is used to replace the diffusion term, which yields these two scenarios

$$\beta C_m \frac{\partial V_m}{\partial t} = \nabla \cdot \boldsymbol{\sigma}_i \nabla \{\Phi_i | V_m\} + I_{\text{foot}} - \beta I_{\text{ion}} \quad (22)$$

or

$$C_m \frac{\partial V_m}{\partial t} = I_{\text{foot}} - I_{\text{ion}}. \quad (23)$$

In the latter formulation the contributions of the diffusion operator towards changing the local transmembrane voltage $V_m(\mathbf{x})$ are fully ignored. This omission is computationally enormously beneficial as the problem of solving the R-E system is reduced to purely local pointwise operations. However, since diffusion plays an important role in smoothing out gradients in V_m during repolarization the total neglect of diffusion may potentially distort the signature of repolarization in electrograms and the ECG to an unacceptable degree. To evaluate the accuracy of these two strategies – referred to as R-E⁺ or R-E⁻ model which considers or ignores diffusion, respectively – relative to a bidomain R-D model the following models were investigated:

R-E⁻ Diffusion is neglected, thus we solve

$$C_m \frac{\partial V_m}{\partial t} = I_{\text{foot}} - I_{\text{ion}}. \quad (24)$$

R-E⁺ Diffusion is taken into account. In order to avoid excess stimulation and distortions of the supra-threshold upstroke phase, an additional threshold condition was applied to I_{foot} :

$$I_{\text{foot}}(\mathbf{x}, t) := \begin{cases} I_{\text{foot}}(t) & \text{if } t \in [t_a(\mathbf{x}) - T_{\text{foot}}, t_a(\mathbf{x})] \text{ and } V_m(\mathbf{x}, t) < V_{\text{th}} \\ 0 & \text{else} \end{cases} \quad (25)$$

where V_{th} is chosen with a given margin of safety above the intrinsic excitation threshold of the cellular dynamics model used. Therefore, $I_{\text{foot}}(\mathbf{x}, t)$ guarantees a *latest* time of activation, but activation can happen earlier due to diffusion currents. The equation we solve is then

$$C_m \frac{\partial V_m}{\partial t} = I_{\text{foot}} + \nabla \cdot \boldsymbol{\sigma}_i \nabla \{\Phi_i | V_m\} - I_{\text{ion}}. \quad (26)$$

Both R-E⁺ and R-E⁻ model were compared to R-D model results to quantify deviations during depolarization and repolarization and to gauge the suitability of these models for predicting potential fields $\Phi_e(\mathbf{x})$ and electrograms.

2.7 Evaluation Benchmarks

The ability of the R-E model to produce accurate activation and repolarization sequences as well as the fidelity of computed electrograms in the near field close to the electrical sources in the myocardium and in the far field at the body surface was evaluated. The evaluation was based on comparing R-E model predictions against gold standard high resolution bidomain R-D models which served as a reference.

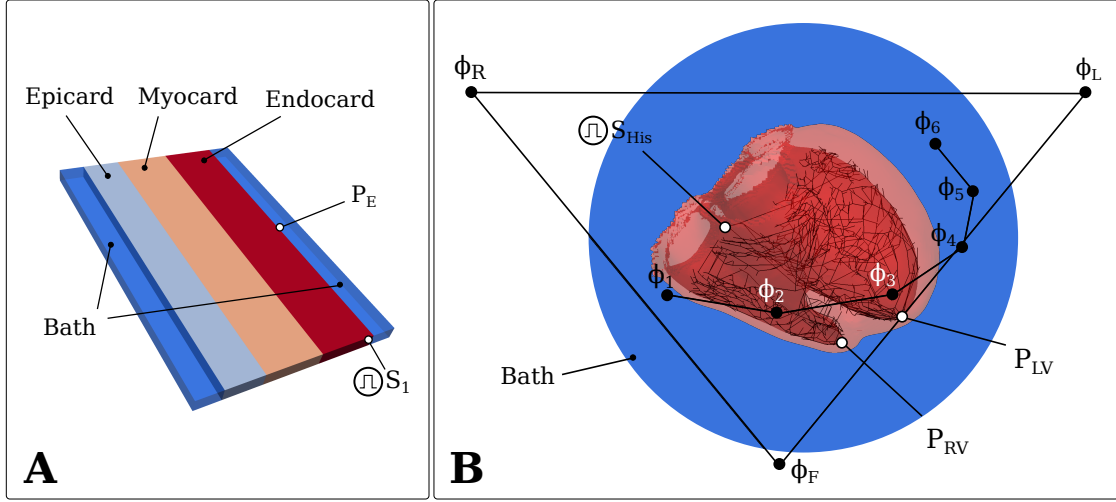


Figure 1: **A)** The wedge geometry with the stimulus S_1 and the sensing electrode with P_E . **B)** The human BiV geometry with the His stimulus S_{His} , the right-ventricular and left-ventricular sensing electrodes P_{RV} and P_{LV} and the ECG electrodes $\Phi_L, \Phi_R, \Phi_F, \Phi_1, \Phi_2, \Phi_3, \Phi_4, \Phi_5, \Phi_6$.

2.7.1 Benchmark Setups

Two setups of different complexity were considered, a geometrically simplified geometry of a transmural wedge preparation and a human biventricular (BiV) geometry equipped with a topologically realistic model of the His-Purkinje system (HPS). Both geometries were immersed in a conductive bath with a conductivity of $\sigma = 1.0 \text{ S/m}$. Fiber architecture was incorporated assuming a linear rotation of fiber angles from -60° at the epicardium to $+60^\circ$ at the endocardium. Tetrahedral finite element meshes were used to discretize the geometries at different spatial resolutions, $dx = 100, 200$ and $400 \mu\text{m}$ for the wedge setup and average discretizations of $dx = 220, 440$ and $880 \mu\text{m}$ for the BiV setup. Details on the construction of the BiV benchmark setup were reported previously [3, 16].

The Ten-Tusscher (TNNP) model [56] was used to describe cellular dynamics of ventricular myocytes. The TNNP model accounts for differences in the transient outward and slow delayed rectifier currents that make up the intrinsic electrophysiological heterogeneity in endocardial, mid-myocardial, and epicardial regions [1]. In the human BiV setup, the ventricular wall consisted of 30% endocardium, 45% midmyocardium and 25% epicardium. In addition to transmural heterogeneity, apicobasal heterogeneity is also known to exist in the heart [55]. In the BiV setup apicobasal heterogeneity was accounted for via an alteration of the slow delayed rectifier potassium current I_{Ks} . In humans, action potential duration is longer at the base than at the apex [55]. To incorporate these characteristics into the benchmark setup, the ventricles were divided into base, mid, and apex regions where I_{Ks} was rescaled by factors of 1.0, 1.25 and 1.5, respectively [28]. Cellular dynamics in the HPS was described by the Stewart et al model of a human Purkinje cell [52].

2.7.2 Activation and Repolarization Sequences

Reference solutions were computed with the highest resolution meshes ($100\mu m$ and $220\mu m$ for wedge and BiV setups, respectively) using both bidomain and pseudo-bidomain R-D models to be compared then against pseudo-bidomain R-E models. In the wedge benchmark, R-E models were solved over the same range of mesh resolutions as the R-D model. If not otherwise noted, in the BiV case resolutions of $dx = 220\mu m$ and $dx = 880\mu m$ were used for R-D and R-E models, respectively. Assuming rotational isotropy of conduction velocities conductivities were chosen close to experimental measurements [46] for the wedge as $g_{il} = 0.16069$, $g_{el} = 0.625$, $g_{it} = 0.04258$ and $g_{et} = 0.236$, and for the BiV setup as $g_{il} = 0.23415$, $g_{el} = 0.22$, $g_{it} = 0.08603$ and $g_{et} = 0.13$, which resulted in conduction velocities of $0.6 m/s$ and $0.3 m/s$ in longitudinal and transverse direction, respectively. These velocities were prescribed in the R-E model simulations for all spatial resolutions. Wavefront propagation in the wedge setup was initiated at time $t = 0$ by delivering a pacing stimulus at the apical endocardial edge of the preparation. In the BiV benchmark, propagation was initiated at time $t = 0$ by stimulating the His bundle (Fig. 1). Metrics used for assessing the quality of the R-E approximation during the activation phase were based on differences between activation maps $t_{a,R-D}$ and $t_{a,R-E}$ as well as temporal features of the upstroke phase of the action potential such as differences in shape between $V_{m,R-D}$ and $V_{m,R-E}$ and rate of rise, $\dot{V}_{m,R-D}$ and $\dot{V}_{m,R-E}$. Activation maps $t_{a,R-D}$ were constructed by using the instant of maximum upstroke velocity, \dot{V}_{max} , as a marker of local activation [51]. Further, at a set of locations the effect of coupling the eikonal-triggered current, $I_{foot}(\mathbf{x}, t)$, upon the shape of foot, upstroke and early repolarization of propagated action potentials was examined. Finally, for gauging the fidelity of the R-E models in reproducing repolarization gradients the spatial distribution of $V_m(\mathbf{x})$ over transmural cross sections of the respective preparations was compared.

2.7.3 Electrograms and ECGs

Subsequent to the evaluation of the R-E model's ability to faithfully represent activation maps $t_a(\mathbf{x})$ and electrical source fields $V_m(\mathbf{x}, t)$, its potential to provide accurate predictions of extracellular potential fields, $\Phi_e(\mathbf{x}, t)$, endocardial/epicardial electrograms as well as ECGs were analyzed. Electrograms as measured with endocardial contact mapping systems, recorded in the vicinity of the endocardium, and non-contact mapping systems, recorded in the blood pool, were simulated in both the simplified wedge benchmark and the anatomically accurate BiV benchmark. The same activation and repolarization sequence simulations were repeated with both R-D and R-E⁺ model using a pseudo-bidomain model as an electrical source representation to compute extracellular potentials $\Phi_{e,R-D}$ and $\Phi_{e,R-E}$, respectively. Further, electrogram traces were compared at the recording sites P_E in the wedge and P_{LV} and P_{LV} in the BiV benchmark (Fig. 1).

In addition to comparing electrograms recorded in the near field close to the myocardial sources ECG recordings were simulated in the BiV benchmark to quantify differences between high resolution R-D model and lower resolution R-E model with regard to extracellular potentials Φ_e in the far field. A simplified ECG model was used based on the assumption of the heart being immersed in an unbounded conductive medium. In this case unipolar extracellular potentials can be recovered by using the integral solution to Poisson's equation

$$\Phi_e(\mathbf{x}_f, t) = \frac{1}{4\pi\sigma} \int_{\Omega_s} \frac{I_m(\mathbf{x}_s, t)}{r_{sf}} d\Omega_s \quad (27)$$

where Φ_e are the potentials at a given field point, \mathbf{x}_f , I_m is the source density at a given source

point, \mathbf{x}_s , and $r_{sf} = \|\mathbf{x}_s - \mathbf{x}_f\|$ is the distance between source and field point [7]. Nine unipolar electrograms, $\Phi_L, \Phi_R, \Phi_F, \Phi_1, \Phi_2, \Phi_3, \Phi_4, \Phi_5, \Phi_6$, were recovered from leads located at the approximated clinical standard electrode positions, $\mathbf{x}_L, \mathbf{x}_R, \mathbf{x}_F, \mathbf{x}_1, \mathbf{x}_2, \mathbf{x}_3, \mathbf{x}_4, \mathbf{x}_5, \mathbf{x}_6$, at the torso surface (Fig. 1). Following [30], a twelve lead clinical standard ECG was derived then including the three Einthoven leads, V_I, V_{II} and V_{III} , the augmented Goldberger leads V_{aVL}, V_{aVR} and V_{aVF} , and the Wilson leads, $V_1, V_2, V_3, V_4, V_5, V_6$.

2.7.4 Computational costs

Execution times for running R-D, R-E⁺ and R-E⁻ model were recorded and broken down into the costs of solving eikonal equation (19), parabolic PDE (7), elliptic PDE (6), the set of ODE's forming the reaction term (4) and of solving Eq.(27) to compute a body surface ECG.

3 Results

3.1 Activation sequence

The ability of the R-E model to approximate activation sequences as computed with a high resolution R-D model was gauged by comparing activation maps $t_a(\mathbf{x})$. If not noted otherwise, a full bidomain formulation is used for the R-D model and a pseudo-bidomain formulation for the R-E models. For the wedge setup discretized at the highest resolution of $dx = 100 \mu m$ a comparison of the maps $t_{a,R-D}(\mathbf{x})$ and $t_{a,R-E^+}(\mathbf{x})$ is shown in Fig. 2A. Fig. 2B highlights differences in activation patterns between two R-D models (bidomain and pseudo-bidomain), as well as between R-D and R-E⁺ model. As previously demonstrated [6], the pseudo-bidomain based activation sequence matches very closely the activation sequence based on the computationally substantially more expensive bidomain model. The maximum deviations were small, ≤ 1 ms and ≤ 3 ms, respectively for the pseudo-bidomain and R-E models.

In contrast to the R-D models, the R-E models do not show any variability in conduction velocity at lower spatial resolutions. Comparing the activation maps shown in Fig. 2C with the bidomain R-D reference solution in Fig. 2A reveals that conduction velocity of the R-D models are appreciably slower when reducing spatial resolution from $100 \mu m$ to $200 \mu m$ and $400 \mu m$ [35] whereas this effect was not witnessed with the R-E models.

These findings were confirmed in the human BiV benchmark where a complex HPS initiated ventricular activation sequence was simulated with a R-D bidomain model and a R-E pseudo-bidomain model. The HPS initiated propagation at the ventricular endocardium at numerous PVJs, leading to a large number of depolarization wavefronts which increasingly amalgamated when traversing the myocardial wall in a transmural direction (Fig. 3A). The excellent agreement between the activation sequences is illustrated in Fig. 3B where activation maps are shown at the anterior epicardium, the posterior endocardium and for basal as well as apical short axis sections.

3.2 Coupling of eikonal model with reaction terms

The effect of coupling the eikonal-triggered current, $I_{foot}(\mathbf{x}, t)$, upon the foot, upstroke and early repolarization of propagated action potentials is illustrated in Fig. 4. Action potential propagation was simulated with R-D, R-E⁺ and R-E⁻ at grids of varying resolutions $dx = 100 \mu m, 200 \mu m$ and $400 \mu m$. The time course of the upstroke of the action potential was recorded at location

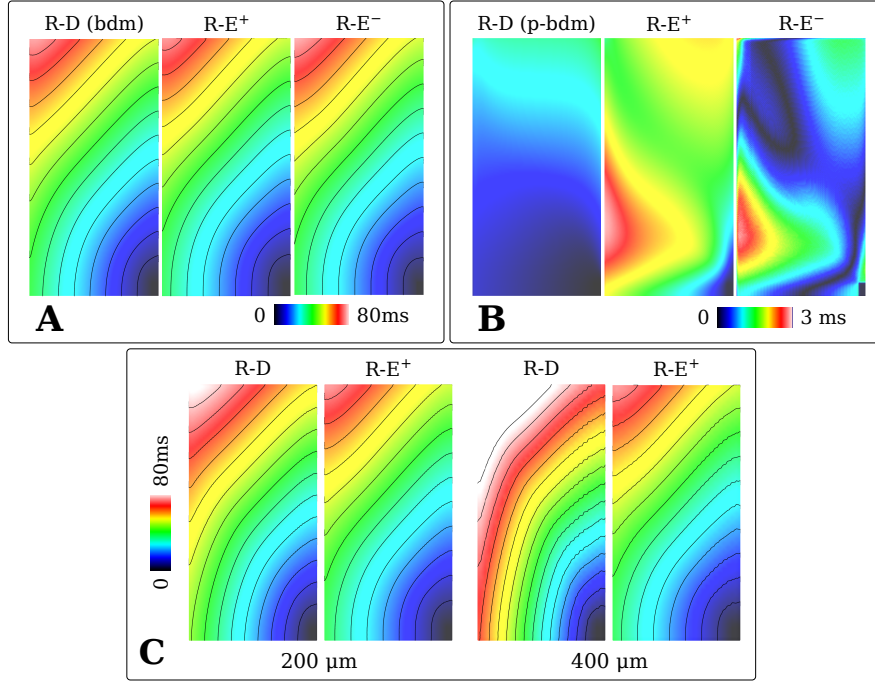


Figure 2: **A)** Activation maps of R-D bidomain (R-D(bdm)), R-E⁺ and R-E⁻ models for the 100 μm wedge benchmark. **B)** Absolute difference in activation times between R-D pseudo-bidomain (R-D (p-bdm)), R-E⁺ and R-E⁻ model to the reference R-D (bdm) model. **C)** Dependence of activation upon spatial discretization. R-D models were sensitive to reducing spatial resolution whereas R-E models remained virtually unaffected.

P_E (Fig. 1A). Time traces obtained with the R-D model feature the known artifacts of reduced conduction velocity with coarser spatial discretization [35] (Fig. 4A). Moreover, at the coarsest resolution of $dx = 400 \mu\text{m}$ additional bumps appeared during the upstroke phase of the action potential due to the inaccurate representation of gradients at coarser spatial resolutions. Minor delays were also witnessed with the R-E⁺ model, albeit to a much lesser degree, however diffusion-mediated bumps during the upstroke phase appeared as well the same way as in the R-D model. At the finer resolutions of 100 and 200 μm the time course of foot and upstroke of the action potential coincided very closely (Fig. 4B). The effect of ignoring diffusion in the R-E⁻ model is highlighted in Fig. 4B. In this case the upstroke is slightly precipitated and the overshoot is overestimated.

3.3 Repolarization sequence

Gradients in transmembrane voltage during repolarization are the sources of extracellularly recorded repolarization signals such as the T-wave in the ECG. The fidelity of the R-E models in replicating these gradients were analyzed at the instant of $\approx 50\%$ repolarization at the center of the wedge preparation (Fig. 5A). Between R-D and R-E⁺ models no appreciable differences were detected as

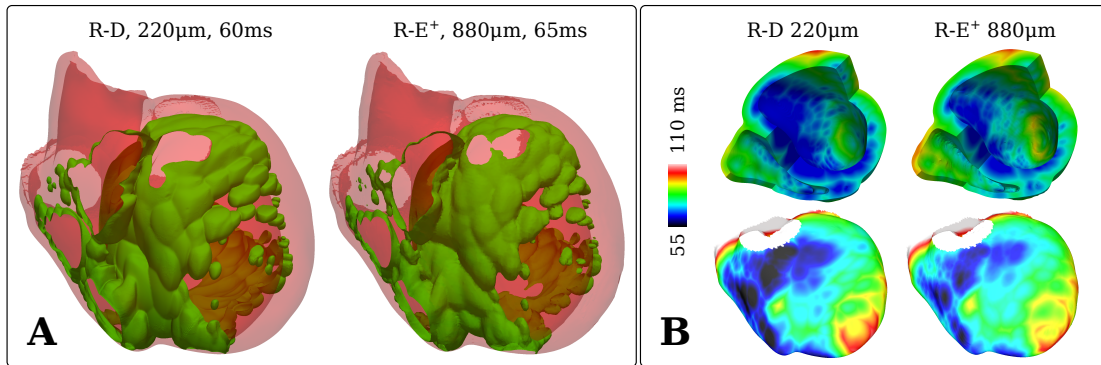


Figure 3: Comparison of activation patterns in the human BiV benchmark with HPS computed with R-D and R-E models at mesh resolutions of $220 \mu m$ and $880 \mu m$, respectively. **A)** Isochronal surfaces computed from the activation maps obtained with the high resolution R-D model and the lower resolution R-E models at time $t = 60 ms$. **B)** Upper panels show activation maps $t_{a,R-D}$ and $t_{a,R-E}$ at the posterior and apical endocardium as well as over basal and apical transmural cross sections in a short axis view. Lower panels compare epicardial activation maps $t_{a,R-D}$ and $t_{a,R-E}$ from an anterior view.

the consideration of the diffusion term in the R-E⁺ model smoothed out intrinsic repolarization gradients exactly the same way as in the R-D model. This was not the case with the R-E⁻ model which neglects diffusion and thus preserves intrinsic gradients. This led to a significant overestimation of spatial gradients across adjacent zones of differing intrinsic action potential duration relative to the R-D model (compare R-D and R-E⁻ panels in Fig. 5B) and also altered temporal dynamics of repolarization noticeably (Fig. 5C).

Similar observations were made in the BiV benchmark where repolarization patterns were compared between the high resolution R-D and the lower resolution R-E model. Fig. 6 illustrates differences in repolarization of R-E⁺ and R-E⁻ relative to the R-D model. Despite a fourfold reduction in spatial resolution the R-E⁺ model yielded virtually identical repolarization patterns. Again, the R-E⁻ model significantly overestimated repolarization gradients around the transitional zones between regions of different intrinsic action potential durations.

3.4 Electrograms and ECG

Extracellular potential fields $\Phi_e(\mathbf{x}, t)$ were computed with R-D, R-E⁺ and R-E⁻ pseudo-bidomain models in both wedge and BiV setup. $\Phi_e(\mathbf{x})$ in the wedge benchmark was visualized during wavefront propagation at $t_d = 27 ms$, the time instance where the activation has just passed P_E (Fig. 7A) as well as during repolarization at $t_d = 320 ms$ (Fig. 7B). Unipolar electrograms recorded at electrode location P_E are shown in Fig. 7C. All models approximated the depolarization phase of the electrogram with sufficient accuracy which resulted in very similar potential fields $\Phi_e(\mathbf{x}, t)$. However, during repolarization the overestimation of spatial gradients of V_m in the R-E⁻ source model due to the absence of diffusion translated into an overestimation of gradients in Φ_e . This is particularly apparent in the late repolarization phase in the electrogram shown in the R-E⁻ panel of Fig. 7C). In contrast, the R-E⁺ model yielded electrograms which were virtually indiscernible from

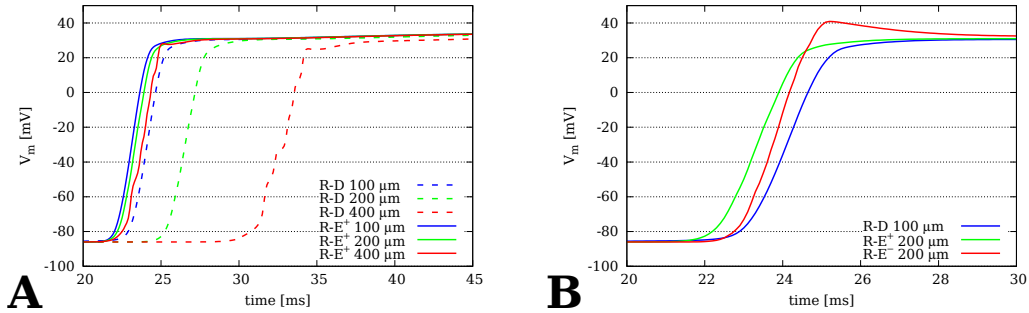


Figure 4: Time traces $V_m(t)$ taken from location P_E at the endocardium of the wedge model. **A)** Comparison between R-D and R-E⁺ model for spatial resolutions of $dx = 100 \mu m$, $200 \mu m$ and $400 \mu m$. **B)** Comparison between gold standard R-D model with R-E⁺ and R-E⁻ model. Ignoring diffusion tends to accelerate upstroke velocity and to enhance the overshoot of the action potential.

those provided by the reference R-D model (compare R-D and R-E⁺ panel in Fig. 7C). This was also the case when using coarser resolutions (compare R-E⁺ and R-E⁺ $400 \mu m$ panels in Fig. 7C).

Analogously, the distribution of $\Phi_e(\mathbf{x})$ for the human BiV benchmark was compared during activation at $t_d = 60 ms$ and repolarization at $t_r = 390 ms$ between R-D and R-E models. As in the wedge case, potential maps $\Phi_e(\mathbf{x}, t_d)$ during depolarization agreed very well between all models. This was not the case for repolarization. While the potential maps $\Phi_e(\mathbf{x}, t_r)$ showed excellent agreement between R-D and R-E⁺ model, noticeable deviations were witnessed for the R-E⁻ model (Fig. 8A). Similarly, this was apparent with electrograms computed at the recording sites P_{LV} and P_{RV} . The depolarization complexes agreed very well between all models whereas the repolarization complexes were qualitatively very similar only between R-D and R-E⁺ model with minor quantitative deviations, but not in the R-E⁻ case where major qualitative discrepancies were witnessed (compare R-E⁺ and R-E⁻ traces in Fig. 6B).

A standard clinical ECG was simulated with R-D, R-E⁺ and R-E⁻ model using the lead system illustrated in Fig. 1. ECG traces of all three models are shown in Fig. 9. Again, ECG traces predicted with the high resolution R-D model and the R-E⁺ and R-E⁻ models using the coarser mesh resolution matched closely for the depolarization phase, however, during repolarization major deviations of the R-E⁻ model were observed.

3.5 Computational costs

Table 1 summarizes the timings recorded for the human BiV benchmark. Execution times incurred for solving the eikonal equation (19) and forward ECG model (27) were insignificant, amounting only to a fraction of the overall setup time and as such there were not explicitly listed. For instance, computing the activation map $t_a(\mathbf{x})$ for the R-E simulations with the $880 \mu m$ human BiV model took only ≈ 7 seconds. The gold standard R-D simulation with a resolution of $dx = 220 \mu m$ required over three orders of magnitude more CPU time as compared to the R-E⁺ simulation at a resolution of $dx = 880 \mu m$.

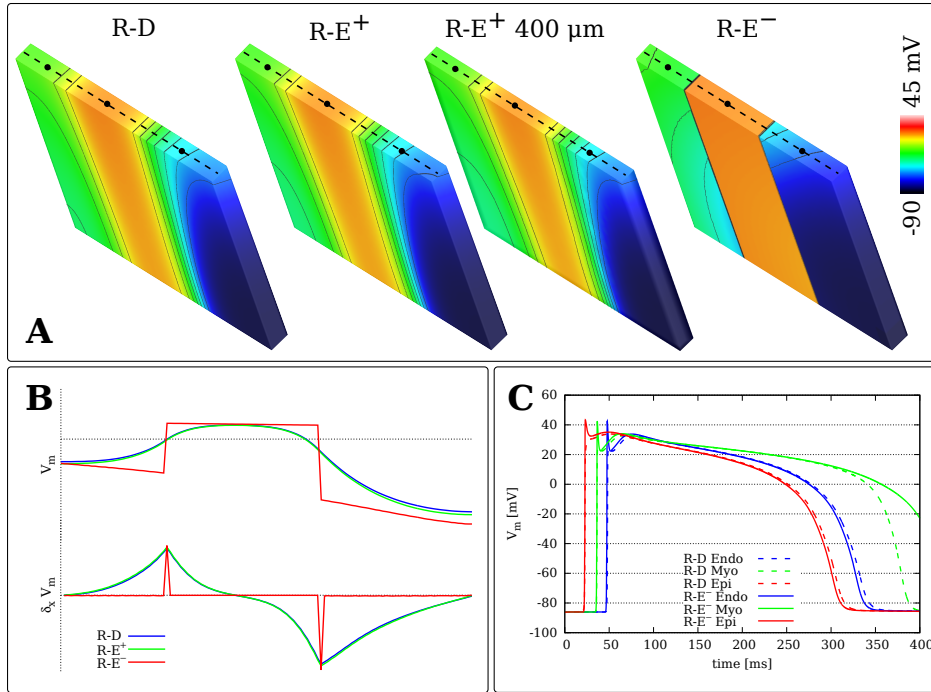


Figure 5: **A)** Differences in transmembrane voltage distribution $V_m(\mathbf{x}_{\text{mid}}, t_{r_{50}})$ over a medial long axis transmural cross section at $t = 305$ ms, the instant of 50% repolarization, at the center of the cross section between R-D, R-E⁺ and R-E⁻ model. The used spatial resolution was 100 μ m. **B)** V_m and its normalized spatial derivative across the center line of the cross section (dashed lines in panel A). **C)** Time traces of action potentials taken along a central transmural line at positions located at the center of endocardial, myocardial and epicardial layer (the black circles on the dashed center lines in panel A) for R-D and R-E⁻ model. R-E⁺ traces are not shown as they are not discernible from the R-D case.

4 Discussion

In this study we describe novel methodology for modeling intracardiac electrograms and ECGs in human organ scale models in a computationally efficient manner. A key requirement for modeling electrograms with a high degree of physiological fidelity is a biophysically accurate representation of bioelectric sources in the heart. The cardiac bidomain model or equivalent computationally cheaper variants [6, 41] are considered to provide the most accurate source representation at mesoscopic (ensembles of cells large enough for homogenization) up to the macroscopic size scales (larger tissue patches up to the organ scale). However, the reaction-diffusion nature of these models imposes accuracy and stability constraints on numerical solution schemes which demand high spatio-temporal resolutions to resolve the fast transients and steep gradients driving the propagation of depolarization wavefronts, rendering bidomain simulations of human hearts computationally vastly expensive [34, 41].

The eikonal equations are an efficient approach for computing activation and repolarization

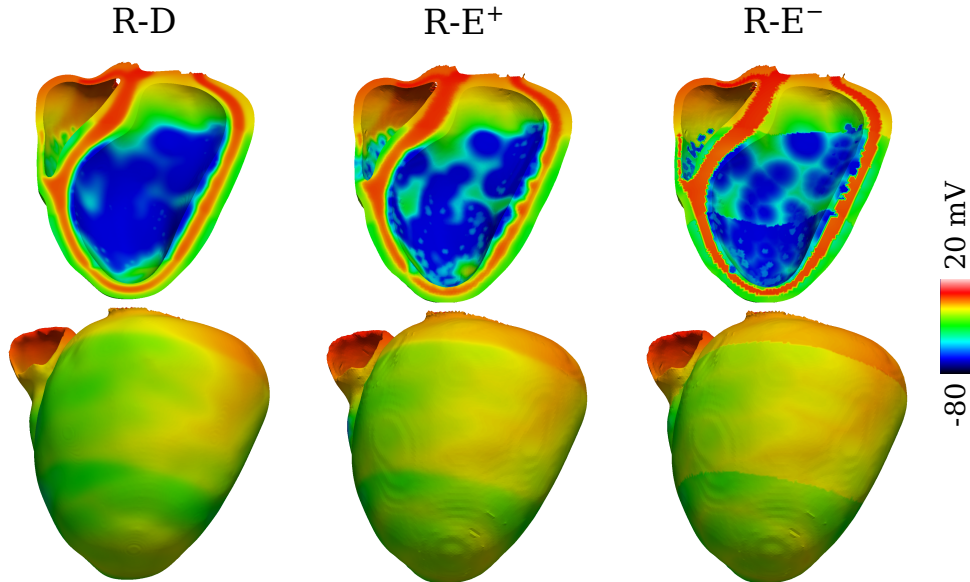


Figure 6: Differences in repolarization between the R-D ($dx=220 \mu m$) and R-E ($dx=880 \mu m$) BiV models at $t = 330 ms$.

sequences in the heart [14, 27, 50, 18], but must be coupled to a source model to represent the biophysical quantities such as V_m , I_m or Φ_i needed to compute electrograms in the interstitial space, within the cavities, at endocardial or epicardial surfaces or at the body surface. To achieve physiologically accurate coupling between instants of activation as provided by an eikonal model with reaction terms describing the electrical sources in a R-E model, a set of conditions must be fulfilled for a R-E model to be as universally applicable as possible. First and most importantly, the difference in electrical activation sequence between R-D and R-E model must be sufficiently small, as activation governs the spatio-temporal behavior of depolarization wavefronts which in turn governs the depolarization complex in electrograms and the ECG. Secondly, the coupling of instants of activations with the reaction term should not distort the upstroke phase, particularly the late

		# d.o.f.	# N_c	Ell.	Par.	ODEs	T_{exec}	T_{CPU}
R-D	$220 \mu m$	46,920,304	1,024	72,227	2,593	735	75,555	$7.8 \cdot 10^7$
R-E ⁺	$880 \mu m$	1,909,531	24	854	476	252	1,582	$3.8 \cdot 10^4$
R-E ⁻	$880 \mu m$	1,909,531	24	867	1	270	1,138	$m2.7 \cdot 10^4$

Table 1: Execution time, T_{exec} , in seconds for R-D and R-E human BiV simulation runs, broken down into compute time dedicated to solving elliptic PDE (Ell.), parabolic PDE (Par.) and set of ODEs. The degrees of freedom (d.o.f.) comprising the linear systems to be solved for the $220 \mu m$ and $880 \mu m$ models, the number of cores, N_c , as well as the used CPU time, T_{CPU} , are given.

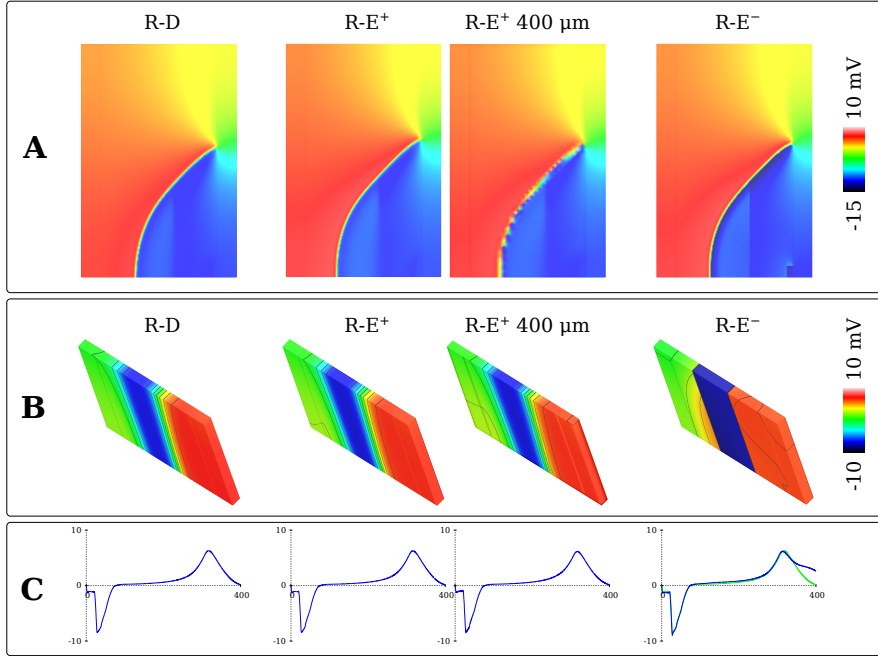


Figure 7: Distribution of $\Phi_e(\mathbf{x})$ during **A)** depolarization at $t_d = 27 \text{ ms}$ and during **B)** repolarization at $t_r = 320 \text{ ms}$ in the wedge benchmark. **C)** Comparison of electrograms $\Phi_e(\mathbf{P}_E, t)$. The electrograms provided by the R-E⁺ model are essentially identical to those obtained with the reference high resolution R-D model, even when coarser resolutions were used (compare R-D and R-E⁺ 400 μm panels).

positively polarized phase, as any distortions there may interfere with the early repolarization phase of the action potential and, thus, alter the spike and dome morphology and influence important cellular signaling processes governing Ca^{2+} handling and excitation-contraction coupling [49, 43]. Thirdly, during repolarization electrotonic currents act to smooth out the intrinsic heterogeneity of cellular dynamics between different regions in the heart. These interactions are not captured by local computation of reaction terms with eikonal-based activation times. However, the accurate representation of repolarization gradients is delicate as these directly influence the morphology of the repolarization signal in electrograms and the T-wave in the ECG. The developed R-E modeling methodology satisfies all of these requirements.

We demonstrate by comparing against a high resolution R-D bidomain simulation in both a simplified wedge benchmark as well as in a human BiV benchmark that i) activation sequences between R-D and R-E model are matched very closely; ii) the upstroke and overall morphology of the action potential remain unaffected by the R-E approach; and, iii) the repolarization patterns between R-D and R-E models agreed sufficiently well. These features combined yield electrograms and ECG of high physiological fidelity which can be computed with significantly reduced computational expenses as compared to a R-D model. These savings are largely attributable to the ability of the R-E model to accurately represent activation sequences with coarser computational meshes. Overall, these features render the R-E model a highly suitable approach for various modeling ap-

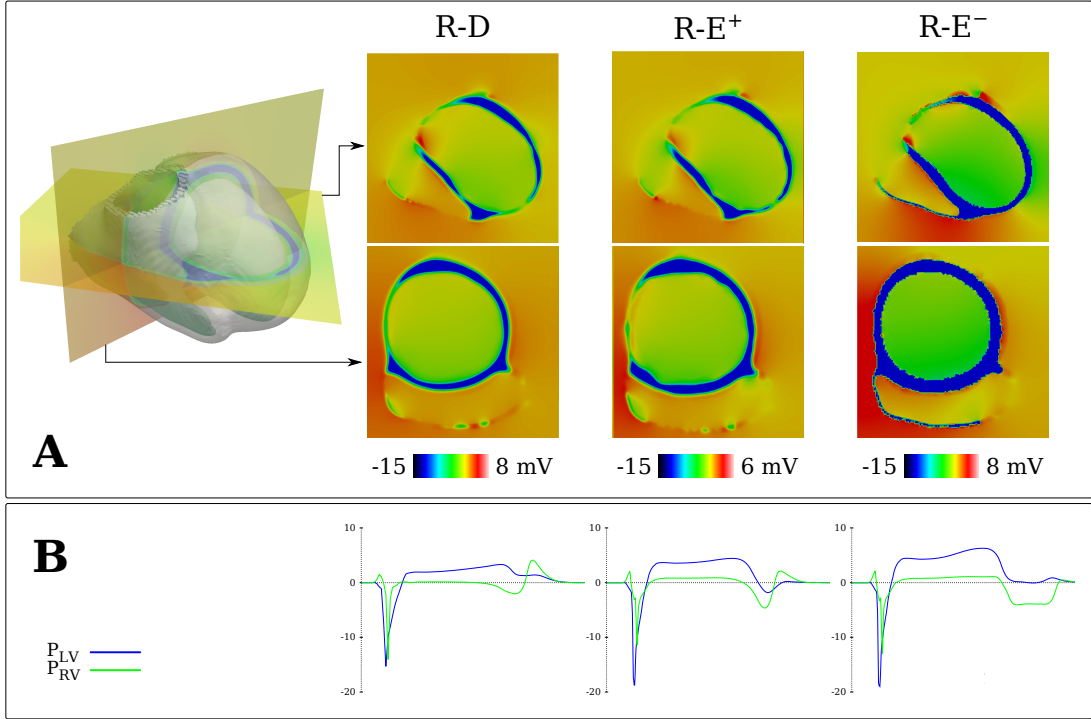


Figure 8: **A** Distribution of extracellular potentials $\Phi_e(\mathbf{x})$ at the instant $t_r = 390$ ms during repolarization. In the leftmost panel frontal and transverse clipping planes used for visualizing $\Phi_e(\mathbf{x})$ are indicated. Right panels compare $\Phi_e(\mathbf{x})$ during repolarization at t_r between high resolution R-D and lower resolution R-E⁺ and R-E⁻ model, respectively. **B** Electrograms recorded at locations P_{LV} and P_{RV} with R-D, R-E⁺ and R-E⁻ model.

plications such as investigating the physics of pacing and sensing or for being used as a forward model in the patient-specific personalization of clinical electrophysiology models. In addition, as all biophysical details of the reaction model are fully preserved, the R-E model is highly suitable as an efficient driver for coupled electro-mechanical simulations which use biophysically detailed coupling between electrophysiology and myofilament model [3].

4.1 Coupling of eikonal model with reaction terms

Eikonal-based activation times must be coupled to a source model to represent the bioelectric sources which generate extracellular potential fields. In general this requires a trigger at time t_a at location \mathbf{x} to initiate an action potential. The method is based on the mathematical description of the foot of a propagated action potential for which we provide the theoretical underpinnings (5). Our method provides a generic mechanism for coupling any model of cellular dynamics with an eikonal-based triggering instant t_a while avoiding any alterations of cellular dynamics due to the coupling terms. This is achieved by using a physiology-based current, I_{foot} , which drives the

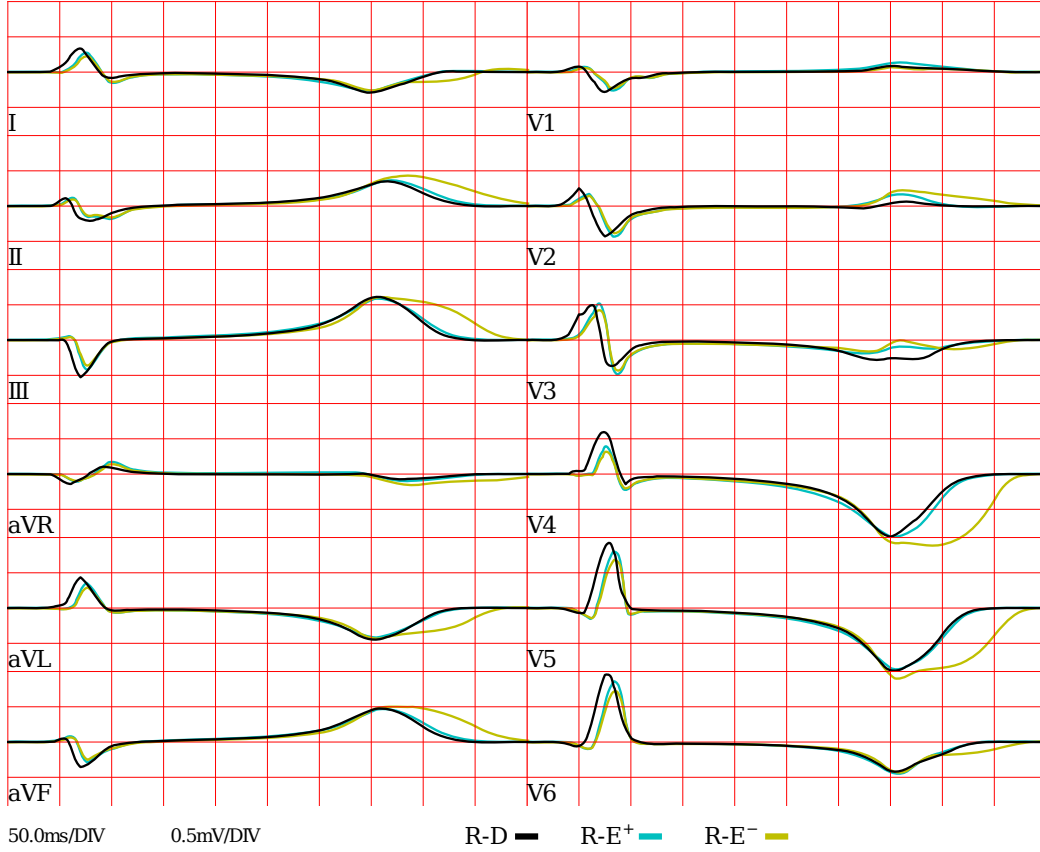


Figure 9: Clinical standard ECG leads computed with R-D, R-E⁺ and R-E⁻ models.

local membrane up to the threshold of sodium channel opening. Characteristic artifacts as they are typically seen in action potential waveforms stimulated with non-physiological currents, are avoided. Specifically, we demonstrate that i) the foot of the action potentials remains essentially unaffected (Fig. 4A-B); ii) upstroke velocity and the action potential morphology of the positively polarized phase of the upstroke were virtually identical between R-D and R-E⁺ model. Preserving the morphology of the positively polarized phase of the upstroke and the early repolarization phase as in the R-D model is of pivotal importance as the action potential morphology during these phases may not only strongly influence the internal state variables of a myocyte model [43], but also alter the J-wave in electrogram recordings [60, 19]. Most importantly, the early repolarization phase sets the plateau voltage level of the action potential, affects action potential duration and intracellular Ca^{2+} concentration and therefore impacts Ca^{2+} handling and excitation-contraction coupling. While the overall action potential morphology may still be comparable, intracellular signaling may be significantly impaired. Similar considerations apply to numerical discretization artifacts which affect the late upstroke phases. For instance, numerical schemes were reported

geared towards facilitating the use of coarser spatio-temporal discretizations [23]. Depending on a chosen discretization, action potential morphologies converged towards reference solutions computed with fine spatio-temporal resolutions, but featured striking oscillations during early repolarization. Such significant deviations for the intrinsic morphology during early repolarization are unacceptable in biophysically detailed modeling studies due to the marked impact upon cellular signaling. In the case of the R-E⁻ model alterations in upstroke waveform were noticed. Due to the absence of diffusion the waveform of the late phase of the upstroke resembles the upstroke observed in an isolated myocyte and thus upstroke velocity is faster and the overshoot is more pronounced. Depending on the specific applications such minor deviations may be acceptable or not.

4.2 Activation sequence

The electrical activation sequence $t_a(\mathbf{x})$ tracks the spatio-temporal patterns of depolarization wavefronts over the myocardium. These patterns represent the bioelectric sources which drive the extracellular potential fields and shape the depolarization complexes in extracellular potential recordings. An accurate description of bioelectric sources relies therefore upon an accurate representation of the activation sequence and the computation of extracellular potential fields in turn relies upon an accurate source model. The location of wavefronts and their spatial profile is directly reflected in the depolarization complexes of electrograms. An accurate source model is therefore key for modeling electrograms with the best possible fidelity, particularly if finer details of electrograms recorded in closer vicinity to the sources at endocardial or epicardial surfaces are under investigation.

As illustrated in Figs. 2 and 3, the R-E model is able to replicate the activation sequence computed with a R-D model at high spatial resolution with high fidelity at lower resolutions at a fraction of the computational costs. The computational gains stem primarily from the ability of the R-E model to accurately represent activation sequences at meshes of coarser spatial resolution. As evidenced in Fig. 2C, in the R-D model conduction velocity, v , decreases with decreasing spatial resolution [35, 15]. At very coarse resolution where the spatial extent of the depolarization wavefront, $\Delta\zeta$, along a given direction of propagation, ζ , is at the same order of magnitude as the chosen spatial discretization, dx , severe distortions of wavefront profiles or even artificial conduction blocks may occur [13]. For a given upstroke duration, ΔT , $\Delta\zeta$ decreases with the conduction velocity along direction ζ , that is, $\Delta\zeta = v \times \Delta T$. This is particularly critical under conditions of slow or decremental conduction where $\Delta\zeta$ may drop well below the length scale of a myocyte. The R-E model is not prone to any resolution-related artefacts such as slowing of wavefront velocities or artificial conduction blocks, as can be witnessed in Fig. 2C. This is at least the case within certain bounds of spatial resolution and cannot be extended to arbitrary coarse meshes as an overly aggressive reduction in spatial resolution will inevitably reduce geometric fidelity and also fail to capture curvature and rotation of fiber and sheet arrangements. The coupling of eikonal-based activation times with reaction terms as implemented in our R-E model ensures that tissue at location \mathbf{x} is activated in the latest at time $t \leq t_a(\mathbf{x})$. A marginally earlier activation is possible in the R-E⁺ case since the combined effect of diffusion and the eikonal-triggered current I_{foot} may precipitate the foot of the action potential such that the threshold of excitation is surpassed earlier than prescribed by the eikonal-based activation time t_a .

4.2.1 Wavefront curvature and bath loading effects

However, subtle differences in activation sequence between R-E and R-D model are expected since the eikonal model used for driving wavefront spread in the coupled R-E model does not capture

all physical effects of the R-D model. In particular, there are three major phenomena impacting the activation sequence that are not accounted for by the R-E model: i) The eikonal model does not account for boundary effects. Wave front propagation accelerates when approaching a sealed end since more charge is available for depolarizing the local membrane as no charge is needed for charging downstream tissue [51]. Further, in the R-E⁻ case, where diffusion is not considered, no normal current flux boundary conditions are imposed and as a consequence, activation isochrones do not meet the boundary at a right angle. Further, minor differences are also expected at sites where propagation is initiated. Relative to uniform conduction observed in tissue areas further away than 5 space constants from any tissue boundary, conduction velocity is slower [51]. ii) Unlike the eikonal curvature model [27] the plain eikonal model [14] used in this study does not account for conduction slowing and acceleration due to changes in source-sink ratio of wavefronts of concave or convex curvature [11]. Thus wavefronts travel at the prescribed velocity along the eigenaxes of the tissue as if the wavefront was planar. iii) Finally, the R-E model does not capture wavefront acceleration effects due to *bath loading* [22, 5, 6, 7]. Due to the higher conductivity of the surrounding medium relative to the interstitial conductivity, the conductivity of the extracellular current path at the tissue-bath interface is higher, which translates into a higher conduction velocity in superficial tissue layers [6]. Depending on factors such as the direction of wavefront propagation, the spatial variation in orthotropy due to fiber and sheet arrangement [21] and the ratio of conductivities between bath and interstitial space [6] wavefront profiles may be significantly altered by bath loading effects with a noticeable impact on electrogram signals. Accounting for bath loading with R-E models can be implemented by assigning faster conduction velocity within a thin tissue layer adjacent to the tissue-bath interface, but the accuracy of such an approach was not evaluated in this study.

Activation sequences as shown in Fig. 2A and C suggest that the impact of bath loading upon wavefront profiles was very minor, despite the use of those conductivity values which were shown to provoke the largest bath loading effect among all the measured interstitial conductivity values reported in the literature [46, 48]. Due to the numerous confounding factors the results presented in this study are not sufficiently complete to support a more general claim that bath loading effects do not impact wavefront profiles under all circumstances of physiological relevance. As we have shown previously [8], striking bath loading effects on transmural wavefront profiles are observed for planar wavefronts propagating in an apicobasal direction in absence of fiber rotation. However, in mammalian hearts where fiber rotation is always present and wavefronts move predominantly in a transmural direction, bath loading effects are largely attenuated with the impact of fiber rotation on wavefront profiles dominating over bath loading effects. This view is further corroborated by simulations with the BiV model (Fig. 3). In these simulations bath loading plays a very minor role in shaping the endocardial activation pattern and virtually no role at all in the epicardial tissue layers as wavefronts propagate there in a direction perpendicular to the surface. In the context of the R-E model bath loading effects can be taken into account by prescribing higher conduction velocities to myocardial surface layer, similar to the previously reported concept of using augmented conductivity tensors in monodomain models [6]. In line with theoretical findings [5], the higher prescribed eikonal conduction velocity within the superficial tissue layers would lead to the same asymptotic wavefront velocity as in the R-D model, but the asymptotic wavefront profile is likely to differ [5]. However, exploring the factors governing bath loading and the ability of R-E models to replicate these effects in detail was beyond the scope of this study.

4.2.2 Purkinje-ventricular junction

The endocardial terminals of the HPS – the Purkinje-ventricular junctions (PVJ) – play a key role in the initiation of the ventricular activation sequence. Due to differences in the physics of coupling the HPS with the ventricles between R-D and R-E models the induced endocardial activation pattern may deviate to some extent. While the topology of the HPS and the locations of the PVJs were exactly identical between the R-D and the R-E model, the transduction of the electrical impulse from the HPS into the ventricles is mediated by different mechanisms. In the R-E models, each PVJ was connected to a single location at the endocardial surface and anterograde and retrograde transduction delays were precisely prescribed. This is not the case with the R-D model where transduction delays are influenced by the electrotonic load on either side of the junctions and by differences in electrophysiological properties [10]. Purkinje junctions occur on a scale finer than the elements in the model and, as such, a PVJ at the macro scale represents a terminal branching of the Purkinje fibre. Thus, properties would be expected to vary between macroscopic PVJ's depending on the particular microscopic PVJ densities. Finally, PVJ properties need to be tuned as a function of finite element size in a R-D model to keep transmission across PVJs constant. This would require analysis at every PVJ and was not performed.

4.3 Repolarization sequence

The repolarization sequence, $t_r(\mathbf{x})$, is determined by the activation sequence $t_a(\mathbf{x})$ and the intrinsic action potential duration $APD(\mathbf{x})$. $APD(\mathbf{x})$ is modulated by electrotonic currents which act to precipitate or delay repolarization (see Fig. 5 B-C). Compared to the duration of the action potential upstroke which lasts only ≈ 1 ms, repolarization is a much slower process lasting for several tens of ms. This translates into a much larger spatial extent of the waveback compared to the spatial extent of the wavefront. The constraints on spatial discretization during repolarization are therefore much more relaxed, facilitating the accurate representation of the spatio-temporal dynamics of wavebacks with much coarser resolutions. Numerical approximation errors are of lesser concern during this phase and as such the exact same discretization schemes can be used in both the R-D and the R-E models. Consequently, aside from minor discrepancies introduced by deviations in activation, the repolarization phase is virtually identical between the R-E⁺ and R-D models (compare R-D and R-E⁺ panels in Fig. 5). This is not the case for the R-E⁻ model though. As the R-E⁻ does not take into account diffusion intrinsic cellular differences in $APD(\mathbf{x})$ are fully preserved, leading to sharp transitions between regions of different cellular dynamics. These sharp transitions act as artificial sources which noticeably influence the repolarization complex in electrograms (Fig. 7 and Fig. 8). However, it is worth noting that the scenario considered in here with sharp transitions in intrinsic properties of cellular dynamics can be considered an extreme case. Gradients in ion channel properties exist in healthy hearts and are exacerbated in disease, but properties vary spatially in a smoother less abrupt fashion [9]. Thus this distinct disadvantage of the R-E⁻ model is likely to play a less prominent role in cases with physiologically more realistic gradients in ion channels. Further, minor differences in repolarization behavior were also observed over the endocardia. These can be attributed to differences in modeling the physics of coupling the HPS with the myocardium via PVJs which is not identical between R-D and R-E models, as elucidated above in Sec. 4.2.2.

4.4 Electrograms and ECG

In general, extracellular potential maps $\Phi_e(\mathbf{x})$ of the R-D model were accurately replicated with both R-E models which was also reflected in a close agreement of the depolarization complexes in the electrograms. This was also the case during repolarization, but only for the R-E⁺ model. The R-E⁻ ignores diffusion and thus intrinsic heterogeneities in action potential waveforms were preserved. This introduced artificial sources which led to major differences in $\Phi_e(\mathbf{x})$ and noticeable distortions of the repolarization complexes in the electrograms.

Similar conclusions can be drawn with regard to modeling a clinical 12-lead ECG. Differences in depolarization complexes were marginal. A minor delay in the onset of the QRS complex as well as a slightly shorter duration of the QRS complex was witnessed in the R-E models. The systematic delayed onset of QRS is largely constant and could be easily compensated, but we refrained from doing so since absolute timings are of lesser relevance in the interpretation of ECG waveforms. The slightly shorter duration of QRS is indicative of an imperfect match of conduction velocities between those naturally emerging in the R-D model and those prescribed in the R-E models. T-waves were virtually indiscernible between R-D and R-E⁺ model in all leads, but major differences appeared in the R-E⁻ based ECG traces in all leads with more significant T-wave amplitudes.

While many salient features of the clinical standard ECGs were replicated by our model such as the progression of R magnitude and the reduction in S magnitude in the unipolar Wilson leads, other features such as concordant T-waves in the Einthoven leads or a Q-wave in lead I were not. Replicating all known ECG features for a regular sinus activation driven activation and repolarization sequence would require modifications of the generic Purkinje system as well as a more detailed modeling of repolarization gradients [28]. However, as the focus of this study was to demonstrate the suitability of the R-E model for replicating extracellular potential fields as produced with the gold standard bidomain model, a detailed reproduction of all known ECG features was beyond the scope.

4.5 Computational costs

In this study we demonstrate the ability of R-E models to replicate extracellularly recorded potential maps and electrograms as computed with the gold standard bidomain model at significantly reduced computational costs. Computational savings stem mainly from the reduced spatial resolution. Further significant reductions in execution times are possible by reducing temporal resolution as well, but this has not been fully explored in this study. R-E models impose significantly weaker constraints upon spatial discretization, h , compared to the R-D model [35, 13]. Artificial h -dependent alterations in conduction velocity and depolarization wave forms are remedied as the coupling of eikonal-based activation maps $t_a(\mathbf{x})$ with reaction terms ensures accurately timed onsets of depolarization, even when using a coarser h . Since accuracy and stability constraints play a much less critical role during the repolarization phases as spatial distribution of potentials are smooth and the rates of change with time are much more than an order of magnitude slower than during depolarization, temporal resolution dt can be reduced with R-E models. In the case of the R-E⁻ model, the choice of dt is only governed by the stability constraints imposed by the ODE integrator and the desired accuracy. With R-E⁻ models in absence of diffusion (see Sec. 2.6) even precomputed time-shifted action potentials can be used as reaction terms. In this scenario the entire system of equations is free of time derivatives thus allowing to solve the system only at the desired temporal output granularity and to reduce the solving of the system of ODE's to a simple table look-up. In the R-E⁻ model all computations are entirely local without any need for com-

munication which furnishes this approach with extremely parallel scalability. The R-E⁺ model is computationally more costly than the R-E⁻ models, but in return allows to represent the entire physics as accurately as the R-D bidomain model. This renders the R-E⁺ model an ideal driver for electro-mechanical simulations in which the coupling between electrophysiology and deformation model shall be represented with full biophysical detail.

Further reductions in h and thus in computational costs may be possible depending on a particular application. With anatomically accurate models such as the human BiV model used in this study the choice of h in the R-E models is dictated by the demands of resolving anatomical features, parameter heterogeneities as well as solution fields with sufficient accuracy. With coarser h the quality of representing potential fields $\Phi_e(\mathbf{x})$ is noticeably diminished leading to jagged and noisy electrograms which cannot be used for further analysis without appropriate filtering (not shown). In our view a choice of $h \leq 1\text{mm}$ is most suitable for R-E models and can be considered a balanced trade-off between compute cost and accuracy.

5 Conclusions

This study presents novel methodology for the efficient computation of electrograms and ECGs in human whole heart simulations. Using the coupled R-E model activation and repolarization sequences and the extracellular potential fields they are generating can be computed with reduced spatio-temporal resolution and, thus, significantly reduced computational costs without compromising on accuracy and electrophysiological fidelity. Extracellular potential maps and electrograms predicted by the R-E model matched very closely – within the margins of uncertainty of such models – with those predicted by the gold standard bidomain R-D model. Computational savings of three orders of magnitude could be achieved. Due to their efficiency R-E models are ideally suitable for forward simulations in clinical modeling studies which attempt to replicate electrophysiological recordings in the clinic or to efficiently personalize electrophysiological model features.

Appendix

The foot of a propagated action potential

Propagation of a planar wavefront along a given direction x in a homogeneous medium can be described by the one-dimensional monodomain equation given as

$$\sigma_x \frac{\partial^2 V_m}{\partial x^2} = \beta \left(C_m \frac{\partial V_m}{\partial t} + I_{\text{ion}} \right). \quad (28)$$

Under such conditions a depolarization wavefront propagates at a sufficient distance to any tissue boundary uniformly at a constant velocity without any spatial variation in the shape of the wavefront. Mathematically, this can be expressed as

$$V_m(x, t) = V_m(x - vt) \quad (29)$$

or, equivalently, as a differential equation by

$$\frac{\partial^2 V_m}{\partial x^2} = \frac{1}{v^2} \frac{\partial^2 V_m}{\partial t^2} \quad (30)$$

where v denotes the conduction velocity of the propagating wavefront. Under subthreshold conditions, that is, the range of transmembrane voltages V_m below the firing threshold, V_{th} , referred to as the foot of the action potential, the membrane behavior is characterized as passive and linear. The transmembrane current I_m is composed then of a capacitive current I_c and an ionic current I_{ion} where $I_{ion} = G_m V_m$ is ohmic. Thus using (28) with (30) the time course of the action potential at any given point in space can be described by

$$\frac{\sigma_x}{\beta G_m v^2} \frac{\partial^2 V_m}{\partial t^2} - R_m C_m \frac{\partial V_m}{\partial t} - V_m = 0. \quad (31)$$

Using the definition of the time constant of the membrane, τ_m , and the space constant along the direction x , λ_x ,

$$\tau_m = R_m C_m; \quad \lambda_x = \sqrt{\frac{\sigma_x}{\beta G_m}} \quad (32)$$

yields the differential equation of the foot of a propagating action potential

$$\left(\frac{\lambda_x}{v}\right)^2 \frac{\partial^2 V_m}{\partial t^2} - \tau_m \frac{\partial V_m}{\partial t} - V_m = 0 \quad (33)$$

for which an analytical solution is found as

$$V_m = A \cdot \exp \left[\left(\frac{\tau_m v^2}{2\lambda_x^2} + \frac{v}{2\lambda_x} \sqrt{\frac{\tau_m^2 v^2}{\lambda_x^2} + 4} \right) t \right] + B \cdot \exp \left[\left(\frac{\tau_m v^2}{2\lambda_x^2} - \frac{v}{2\lambda_x} \sqrt{\frac{\tau_m^2 v^2}{\lambda_x^2} + 4} \right) t \right]. \quad (34)$$

In the case of a propagating depolarization wavefront the foot of the action potential traverses its rising phase implying that $B = 0$ must hold. Further, in general the assumption $\tau_m^2 v^2 / \lambda_x^2 \gg 4$ holds, allowing to represent the foot of the action potential as a mono-exponential process

$$V_m = A e^{kt} \quad \text{with} \quad k = \frac{\tau_m v^2}{\lambda_x^2} = \frac{1}{\tau_F}, \quad (35)$$

where τ_F denotes the time constant of the foot of the action potential. The time constant τ_F can be determined experimentally [37] or from a simulated propagated action potential through phase plane analysis (Fig. 10). At the arrival time of a propagating depolarization wavefront at the location x in space, $t_a(x)$, the change in transmembrane voltage during the foot of the action potential is described by a function

$$V_m(x, t) = \left[A \cdot e^{\frac{t-t_a(x)}{\tau_F}} + B \right] \cdot \varepsilon_{on}(t - t_a(x)) \cdot \varepsilon_{off}(t_{th}(x) - t), \quad (36)$$

where ε_{on} and ε_{off} are step functions delimiting the time interval $[t_a(x), t_{th}(x)]$ of the foot of the action potential marking the onset of the AP foot and the instant of V_m crossing a given transmembrane voltage threshold at location x . The change of V_m during the foot is driven by the foot current I_{foot} given as

$$I_{foot} = I_{ion} - \nabla \cdot \boldsymbol{\sigma} \nabla V_m = -C_m \frac{dV_m}{dt} = -\frac{A}{\tau_F} \cdot e^{\frac{t-t_a(x)}{\tau_F}} \cdot \varepsilon(t - t_a(x)) \cdot \varepsilon(t_{th}(x) - t). \quad (37)$$

which represents the combined effect of electronic currents due to diffusion, represented by $\nabla \cdot \sigma \nabla V_m$, and the ionic currents, I_{ion} where $I_{\text{ion}} \approx 0$ can be assumed during the foot phase of an action potential. The constant A of the current I_{foot} can be determined by fitting the function in Eq. (37) to the foot of a propagated action potential (Fig. 10).

According to Eq. (35) τ_F depends on the velocity of propagation, suggesting that the foot of the action potential may vary as a function of direction of propagation. However, taking into account the known proportionality relation for conduction velocity

$$v_x \propto K \sqrt{\frac{\sigma}{\beta}} \quad (38)$$

it becomes apparent that λ_x and v_x are related through a constant factor $K/\sqrt{G_m}$ and thus these terms cancel out in Eq. (35).

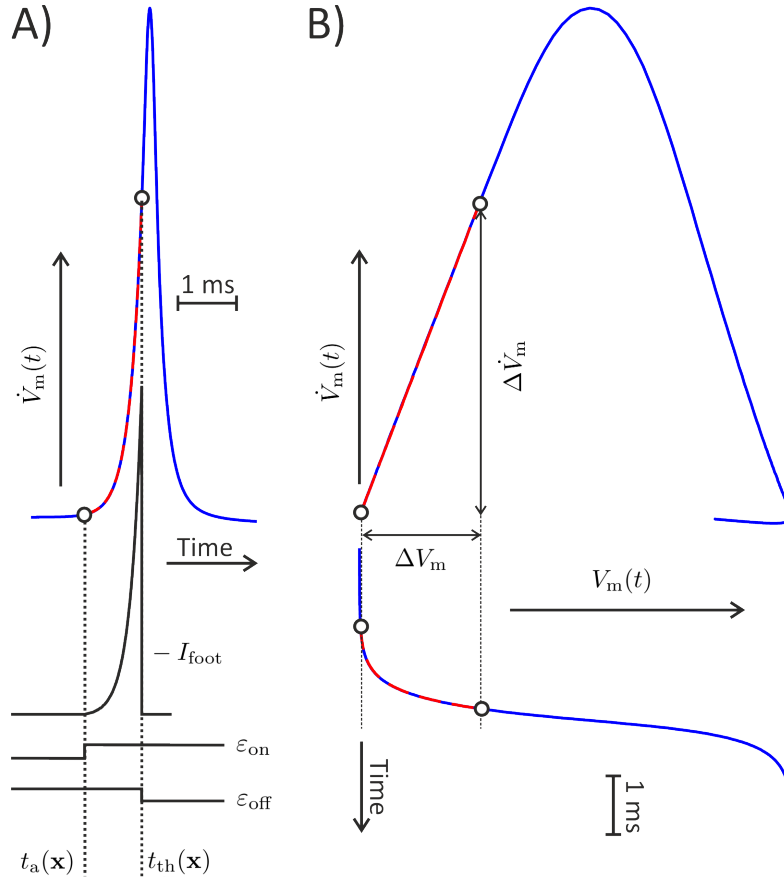


Figure 10: Fitting of current I_{foot} . Shown are traces derived from a simulated propagated action potential (solid blue lines) and traces derived from the fitted current I_{foot} (red dashed lines). Fitting yielded $A = 0.91 \text{ mV}$ and $\tau_F = 0.25 \text{ ms}$. A) Trace of \dot{V}_m , foot current $-I_{\text{foot}}/C_m$ and the step functions $\varepsilon_{\text{on}} = \varepsilon(t - t_a(x))$ and $\varepsilon_{\text{off}} = \varepsilon(t_{\text{th}}(x) - t)$. B) Phase plane trajectory of propagated action potential. During the foot of the action potential the ratio $\Delta \dot{V}_m / \Delta V_m$ is \approx constant

References

- [1] C Antzelevitch and J Fish. Electrical heterogeneity within the ventricular wall. *Basic Res Cardiol*, 96:517–527, 2001.
- [2] Hermenegild J. Arevalo, Fijoy Vadakkumpadan, Eliseo Guallar, Alexander Jebb, Peter Malamas, Katherine C. Wu, and Natalia A. Trayanova. Arrhythmia risk stratification of patients after myocardial infarction using personalized heart models. *Nat Commun*, 7:11437, 2016.
- [3] Christoph M. Augustin, Aurel Neic, Manfred Liebmann, Anton J. Prassl, Steven A. Niederer, Gundolf Haase, and Gernot Plank. Anatomically accurate high resolution modeling of human whole heart electromechanics: A strongly scalable algebraic multigrid solver method for nonlinear deformation. *J Comput Phys*, 305:622–646, Jan 2016.

- [4] Satish Balay, Kris Buschelman, Victor Eijkhout, William D. Gropp, Dinesh Kaushik, Matthew G. Knepley, Lois Curfman McInnes, Barry F. Smith, and Hong Zhang. PETSc users manual. Technical Report ANL-95/11 - Revision 3.0.0, Argonne Nat. Lab., 2008.
- [5] Olivier Bernus and Edward Vigmond. Asymptotic wave propagation in excitable media. *Physical Review E*, 92(1):010901, 2015.
- [6] M J Bishop and G Plank. Representing cardiac bidomain bath-loading effects by an augmented monodomain approach: Application to complex ventricular models. *IEEE Trans Biomed Eng*, page in press, 2011.
- [7] Martin J. Bishop and Gernot Plank. Bidomain ecg simulations using an augmented monodomain model for the cardiac source. *IEEE Trans Biomed Eng*, 58(8), Aug 2011.
- [8] Martin J Bishop, Edward Vigmond, and Gernot Plank. Cardiac bidomain bath-loading effects during arrhythmias: interaction with anatomical heterogeneity. *Biophysical journal*, 101:2871–2881, Dec 2011.
- [9] Boukens BJ, Sulkin MS, Gloschat CR, Ng FS, Vigmond EJ, and Efimov IR. Transmural apd gradient synchronizes repolarization in the human left ventricular wall. *Cardiovasc Res*, 108(1):188–96, 2015.
- [10] Patrick M. Boyle, Makarand Deo, Gernot Plank, and Edward J. Vigmond. Purkinje-mediated effects in the response of quiescent ventricles to defibrillation shocks. *Annals of biomedical engineering*, 38(2):456–468, February 2010.
- [11] Cabo C, Pertsov AM, Baxter WT, Davidenko JM, Gray RA, and Jalife J. Wave-front curvature as a cause of slow conduction and block in isolated cardiac muscle. *Circ Res.*, 75(6):1014–1028, 1994.
- [12] Vergara C, Lange M, Palamara S, Lassila T, Frangi AF, and Quarteroni A. A coupled 3d–1d numerical monodomain solver for cardiac electrical activation in the myocardium with detailed purkinje network. *J Comput Phys*, 308:218–238, 2016.
- [13] R H Clayton, O Bernus, E M Cherry, H Dierckx, F H Fenton, L Mirabella, A V Panfilov, F B Sachse, G Seemann, and H Zhang. Models of cardiac tissue electrophysiology: progress, challenges and open questions. *Progress in biophysics and molecular biology*, 104:22–48, Jan 2011.
- [14] P. Colli Franzone, L. Guerri, and S. Rovida. Wavefront propagation in an activation model of the anisotropic cardiac tissue: asymptotic analysis and numerical simulations. *J Math Biol*, 28(2):121–176, 1990.
- [15] Caroline M. Costa, Hoetzl Elena, Rocha Bernardo M., Prassl Anton J., and Plank Gernot. Automatic parameterization strategy for cardiac electrophysiology simulations. *Comput Cardiol*, 40:373–376, 2013.
- [16] A. Crozier, C. M. Augustin, A. Neic, A. J. Prassl, M. Holler, T. E. Fastl, A. Hennemuth, K. Bredies, T. Kuehne, M. J. Bishop, S. A. Niederer, and G. Plank. Image-based personalization of cardiac anatomy for coupled electromechanical modeling. *Ann Biomed Eng*, 44(1):58–70, Jan 2016.

- [17] Huelsing DJ, Spitzer KW, Cordeiro JM, and Pollard AE. Conduction between isolated rabbit purkinje and ventricular myocytes coupled by a variable resistance. *Am J Physiol*, 274:H1163–H1173, 1998.
- [18] Zhisong Fu, Robert M Kirby, and Ross T Whitaker. A fast iterative method for solving the eikonal equation on tetrahedral domains. *SIAM Journal on Scientific Computing*, 35(5):C473–C494, 2013.
- [19] K Gima and Y Rudy. Ionic current basis of electrocardiographic waveforms: A model study. *Circ Res*, 90:889–896, 2002.
- [20] Gundolf Haase, Manfred Liebmann, Craig C. Douglas, and Gernot Plank. A parallel algebraic multigrid solver on graphics processing units. In Wu Zhang, Zhangxin Chen, Craig C. Douglas, and Weiqin Tong, editors, *HPCA (China), Revised Selected Papers*, volume 5938 of *Lecture Notes in Computer Science*, pages 38–47. Springer, 2009.
- [21] Patrick A Helm, Hsiang-Jer Tseng, Laurent Younes, Elliot R McVeigh, and Raimond L Winslow. Ex vivo 3d diffusion tensor imaging and quantification of cardiac laminar structure. *Magnetic resonance in medicine*, 54:850–859, Oct 2005.
- [22] C S Henriquez, A L Muzikant, and C K Smoak. Anisotropy, fiber curvature, and bath loading effects on activation in thin and thick cardiac tissue preparations: simulations in a three-dimensional bidomain model. *J Cardiovasc Electrophysiol*, 7:424–44, 1996.
- [23] Whiteley J. An efficient numerical technique for the solution of the monodomain and bidomain equations. *IEEE Transactions on Bio-medical Engineering*, 53(11):2139–2147, 2006.
- [24] Vincent Jacquemet. An eikonal-diffusion solver and its application to the interpolation and the simulation of reentrant cardiac activations. *Computer Methods and Programs in Biomedicine*, 108(2):548–558, 2012.
- [25] G. Karypis and V. Kumar. A fast and high quality multilevel scheme for partitioning irregular graphs. *SIAM J. Sci. Comput.*, 20(1):359–392 (electronic), 1998.
- [26] George Karypis, Kirk Schloegel, and Vipin Kumar. Parmetis: Parallel graph partitioning and sparse matrix ordering library. *Version 1.0, Dept. of Computer Science, University of Minnesota*, 1997.
- [27] J. P. Keener. An eikonal-curvature equation for action potential propagation in myocardium. *J Math Biol*, 29(7):629–651, 1991.
- [28] David U J. Keller, Daniel L. Weiss, Olaf Dossel, and Gunnar Seemann. Influence of i(ks) heterogeneities on the genesis of the t-wave: a computational evaluation. *IEEE Trans Biomed Eng*, 59(2):311–322, Feb 2012.
- [29] Manfred Liebmann. Efficient pde solvers on modern hardware with applications in medical and technical sciences. *PhD in natural sciences, Institute of Mathematics and Scientific Computing–Karl Franzens University Graz*, 2009.
- [30] Jaakko Malmivuo and Robert Plonsey. *Bioelectromagnetism - Principles and Applications of Bioelectric and Biomagnetic Fields*. Oxford University Press, 1995.

- [31] A. Neic, M. Liebmann, E. Hoetzel, L. Mitchell, E. J. Vigmond, G. Haase, and G. Plank. Accelerating cardiac bidomain simulations using graphics processing units. *IEEE Trans Biomed Eng*, 59(8):2281–2290, Aug 2012.
- [32] A. Neic, M. Liebmann, E. Hoetzel, L. Mitchell, E. J. Vigmond, G. Haase, and G. Plank. Accelerating cardiac bidomain simulations using graphics processing units. *IEEE Trans Biomed Eng*, 59(8):2281–2290, 2012.
- [33] S Nieder, G Plank, P Chinchapatnam, M Ginks, P Lamata, K Rhode, C Rinaldi, R Razavi, and NP Smith. Length-dependent tension in the failing heart and the efficacy of cardiac resynchronisation therap. *Cardiovasc Res*, 2011.
- [34] Steven Niederer, Lawrence Mitchell, Nicolas Smith, and Gernot Plank. Simulating human cardiac electrophysiology on clinical time-scales. *Front Physiol*, 2:14, 2011.
- [35] Steven A. Niederer, Eric Kerfoot, Alan P. Benson, Miguel O. Bernabeu, Olivier Bernus, Chris Bradley, Elizabeth M. Cherry, Richard Clayton, Flavio H. Fenton, Alan Garny, Elvio Heidenreich, Sander Land, Mary Maleckar, Pras Pathmanathan, Gernot Plank, José F. Rodríguez, Ishani Roy, Frank B. Sachse, Gunnar Seemann, Ola Skavhaug, and Nic P. Smith. Verification of cardiac tissue electrophysiology simulators using an n-version benchmark. *Philos Trans A Math Phys Eng Sci*, 369(1954):4331–4351, Nov 2011.
- [36] Bjørn Fredrik Nielsen, Tomas Syrstad Ruud, Glenn Terje Lines, and Aslak Tveito. Optimal monodomain approximations of the bidomain equations. *Applied Mathematics and Computation*, 184:276–290, 2007.
- [37] A. P. Paes de Carvalho, B. F. Hoffman, and W. B. Langan. Two components of the cardiac action potential. *Nature*, 211(5052):938–940, Aug 1966.
- [38] Ali Pashaei, Daniel Romero, Rafael Sebastian, Oscar Camara, and Alejandro F Frangi. Fast multiscale modeling of cardiac electrophysiology including purkinje system. *IEEE Transactions on Biomedical Engineering*, 58(10):2956–2960, 2011.
- [39] G. Plank, M. Liebmann, R. Weber dos Santos, E. J. Vigmond, and G. Haase. Algebraic multigrid preconditioner for the cardiac bidomain model. *IEEE Trans Biomed Eng*, 54(4):585–96, 2007.
- [40] Gernot Plank, Lufang Zhou, Joseph L Greenstein, Sonia Cortassa, Raimond L Winslow, Brian O’Rourke, and Natalia A Trayanova. From mitochondrial ion channels to arrhythmias in the heart: computational techniques to bridge the spatio-temporal scales. *Philosophical Transactions of the Royal Society A: Mathematical, Physical and Engineering Sciences*, 366(1879):3381–3409, 2008.
- [41] Mark Potse, Bruno Dubé, Jacques Richer, Alain Vinet, and Ramesh M Gulrajani. A comparison of monodomain and bidomain reaction-diffusion models for action potential propagation in the human heart. *IEEE transactions on bio-medical engineering*, 53:2425–35, 2006.
- [42] Mark Potse, Dorian Krause, Wilco Kroon, Romina Murzilli, Stefano Muzzarelli, François Regoli, Enrico Caiani, Frits W. Prinzen, Rolf Krause, and Angelo Auricchio. Patient-specific modelling of cardiac electrophysiology in heart-failure patients. *Europace*, 16 Suppl 4:iv56–iv61, Nov 2014.

- [43] He Q., Feng Y., and Wang Y. Transient outward potassium channel: a heart failure mediator. *Heart failure reviews*, 20(3):349–362, 2015.
- [44] Z. Qu and A. Garfinkel. An advanced algorithm for solving partial differential equation in cardiac conduction. *IEEE Trans Biomed Eng*, 46(9):1166–8, 1999.
- [45] David F. Richards, James N. Glosli, Erik W. Draeger, Arthur A. Mirin, Bor Chan, Jean-Luc Fattebert, William D. Krauss, Tomas Ooppelstrup, Chris J. Butler, John A. Gunnels, Viatcheslav Gurev, Changhoan Kim, John Magerlein, Matthias Reumann, Hui-Fang Wen, and John Jeremy Rice. Towards real-time simulation of cardiac electrophysiology in a human heart at high resolution. *Comput Methods Biomech Biomed Engin*, 16(7):802–805, 2013.
- [46] D E Roberts and A M Scher. Effect of tissue anisotropy on extracellular potential fields in canine myocardium in situ. *Circulation Research*, 50:342–51, 1982.
- [47] Bernardo M. Rocha, Ferdinand Kickingger, Anton J. Prassl, Gundolf Haase, Edward J. Vigmond, Rodrigo Weber dos Santos, Sabine Zaglmayr, and Gernot Plank. A macro finite-element formulation for cardiac electrophysiology simulations using hybrid unstructured grids. *IEEE Trans Biomed Eng*, 58(4):1055–1065, 2011.
- [48] B. J. Roth. Electrical conductivity values used with the bidomain model of cardiac tissue. *IEEE Trans Biomed Eng*, 44(4):326–328, Apr 1997.
- [49] R Sah, Ramirez R J, Kaprielian R, and Backx P H. Alterations in action potential profile enhance excitation – contraction coupling in rat cardiac myocytes. *J Physiol*, 533(1):201–214, 2001.
- [50] M. Sermesant, Y. Coudière, V. Moreau-Villèger, K. S. Rhode, D L G. Hill, and R. S. Razavi. A fast-marching approach to cardiac electrophysiology simulation for xmr interventional imaging. *Med Image Comput Comput Assist Interv*, 8(Pt 2):607–615, 2005.
- [51] M. S. Spach and J. M. Kootsey. Relating the sodium current and conductance to the shape of transmembrane and extracellular potentials by simulation: effects of propagation boundaries. *IEEE Trans Biomed Eng*, 32(10):743–755, Oct 1985.
- [52] P Stewart, OV Aslanidi, D Noble, PJ Noble, MR Boyett, and Zhang H. Mathematical models of the electrical action potential of purkinje fibre cells. *Philos Trans A Math Phys Eng Sci.*, 367(1896):2225–55., 2009.
- [53] G. Strang. On the construction and comparison of difference scheme. *SIAM Journal on Numerical Analysis*, 5:506–517, 1968.
- [54] J. Sundnes, G. T. Lines, and A. Tveito. An operator splitting method for solving the bidomain equations coupled to a volume conductor model for the torso. *Math Biosci*, 194(2):233–48, 2005.
- [55] N Szentadrassy, T Banyasz, T Biro, G Szabo, B I Toth, J Magyar, J Lazar, A Varro, L Kovacs, and P. P. Nanasi. Apico-basal inhomogeneity in distribution of ion channels in canine and human ventricular myocardium. *Cardiovasc Res*, 65:851–860, 2005.

- [56] K H W J ten Tusscher and A V Panfilov. Alternans and spiral breakup in a human ventricular tissue model. *American Journal of Physiology - Heart and Circulatory Physiology*, 291(3):H1088–H1100, 2006.
- [57] E Vigmond, M Hughes, G Plank, and L Leon. Computational tools for modeling electrical activity in cardiac tissue. *J Electrocardiol*, 36:69–74, 2003.
- [58] E. J. Vigmond, R. Weber dos Santos, A. J. Prassl, M. Deo, and G. Plank. Solvers for the cardiac bidomain equations. *Prog Biophys Mol Biol*, 96(1-3):3–18, 2008.
- [59] Edward J Vigmond and Clyde Clements. Construction of a computer model to investigate sawtooth effects in the purkinje system. *IEEE Trans Biomed Eng*, 54(3):389–399, 2007.
- [60] G X Yan and C Antzelevitch. Cellular basis for the electrocardiographic j wave. *Circulation*, 93(2):372–379, 1996.